COMMUNICATION

Check for updates

Selective visible-light driven highly efficient photocatalytic reduction of CO_2 to C_2H_5OH by two-dimensional Cu_2S monolayers†

Shiyan Wang, Xiaowan Bai, Qiang Li, [ID] Yixin Ouyang, [ID] Li Shi and Jinlan Wang [ID] *

Solar-driven highly-efficient photocatalytic reduction of CO_2 into value-added fuels has been regarded as a promising strategy to assuage the current global warming and energy crisis, but developing highly product-selective, long-term stable and low-cost photocatalysts for C_2 production remains a grand challenge. Herein, we demonstrate that two-dimensional β- and δ-phase Cu_2S monolayers are promising photocatalysts for the reduction of CO_2 into C_2H_5OH. The calculated potential-limiting steps for the CO_2 reduction reaction (CO_2RR) are less than 0.50 eV, while those for the hydrogen evolution reaction are as high as 1.53 and 0.87 eV. Most strikingly, the C–C coupling only needs to overcome an ultra-low kinetic barrier of ~0.30 eV, half of that on the Cu surface, indicating that they can boost the C_2H_5OH conversion efficiency greatly. Besides, these catalysts also exhibit satisfactory band edge positions and suitable visible light absorption, rendering them ideal for the visible light driven CO_2RR. Our work not only provides a promising photocatalyst for achieving the efficient and selective CO_2RR, but also brings new opportunities for advanced sustainable C_2H_5OH product.

New concepts

Capture and conversion of CO_2 into value-added fuels has been regarded as a promising strategy to assuage the current global warming and energy crisis, but developing highly product-selective, long-term stable and low-cost photocatalysts for C_2 production remains a grand challenge. Based on the fact that low-coordinated Cu^+ surface atoms enhance CO* binding and S atoms suppress the HER, they hold promising prospects for boosting both the activity and product selectivity. Herein, for the first time, we report a two-dimensional Cu^+ based catalyst, Cu_2S monolayers, as a very compelling photocatalyst for the CO_2RR into C_2H_5OH by means of state-of-the-art DFT calculations. The calculated potential-limiting step for the CO_2RR is less than 0.50 eV, while that for the HER is higher than 0.87 eV. Meanwhile, the C–C coupling only needs to overcome an ultra-low kinetic barrier of ~0.30 eV, half of that on the Cu surface, indicating that the catalyst can boost the C_2H_5OH conversion efficiency greatly. Besides, the catalysts also exhibit satisfactory band edge positions and suitable visible light absorption, rendering them ideal for visible light driven CO_2RR. Our work not only provides a promising photocatalyst for achieving the efficient and selective CO_2RR, but also provides new insights into the development of novel photocatalysts.

Introduction

The development of artificial photosynthesis that captures and converts carbon dioxide (CO_2) into fuels and value-added chemicals by solar energy has drawn increasing attention due to the energy crisis and global warming.[1–3] Recently, conversion of CO_2 to gaseous carbon products of CO,[4,5] CH_4[6,7] and C_1 liquid products, such as HCOOH[8,9] and CH_3OH,[10,11] has been achieved in photocatalytic strategies with high reaction rate. In contrast, reports on the photocatalytic CO_2RR to C_2 products are very limited. In fact, the C_2 liquid alcohol products are more desirable for a wide range of applications in transportation and the chemical industry due to their higher energy density and commercial value than C_1 products.[12–14] However, the selectivity

of the products of the CO_2RR is uncontrollable[15–17] and it suffers from the competing hydrogen evolution reaction (HER)[18,19] as well. Besides, the catalytic CO_2RR to C_2 products with a low kinetic barrier is still a challenge because the C–C coupling is very difficult. Meanwhile, to be a good photocatalyst, satisfactory visible-light absorption and suitable band edge positions are required while current photocatalysts are often suffering from high electron–hole recombination rates and poor visible-light absorption in the wide-bandgap semiconductor materials.[20] Therefore, the development of highly active semiconductor photocatalysts with high product selectivity to achieve efficient photocatalytic CO_2RR is very desirable but rather challenging.

During the CO_2RR process, it is hard to achieve a significantly low free energy barrier because the scaling relation of the adsorption energies between CO* and CHO* intermediates imposes a fundamental limitation on the catalytic efficiency.[21] Some approaches to break this limitation have been proposed: (i) introducing a covalent character of p-orbitals of main-group

*School of Physics, Southeast University, Nanjing 211189, China.
E-mail: jlwang@seu.edu.cn*

† Electronic supplementary information (ESI) available. See DOI: 10.1039/d1nh00196e

elements,[22] (ii) transition-metal atom doping,[23] (iii) designing a special interfacial catalyst motif,[24] (iv) alloying metal catalysts,[25] and (v) adopting a different mechanism without formation of CO*/CHO*.[26] By removing this limitation, the CHO* is independently stabilized over CO*, thus deviating from the scaling relation of transition-metals. To date, copper is one of the most up and coming candidates for the CO_2RR into C_2 hydrocarbons and oxygenates.[27,28] However, the high overpotential and the C–C coupling kinetic barrier cause the low faradaic efficiency and the poor selectivity of C_2 products. One of the most promising approaches to boost both the efficiency and selectivity for the CO_2RR to multi-carbon alcohols is mostly based on copper(ı) species. The surface Cu^+ could modify the surface structure of copper(ı)-based catalysts and promote the CO*–CO* hydrogenation[13,29,30] and C–C coupling reaction,[31] thereby improving the faradaic efficiency for C_2 products.

Very recently, an ultrathin two-dimensional (2D) β-phase Cu_2S bilayer has been successfully synthesized in the laboratory[32–34] and a 2D δ-phase Cu_2S monolayer has also been predicted theoretically[35,36] with superior oxidation resistance, ultrahigh carrier mobility and excellent thermodynamic stability. Importantly, the p-type semiconducting Cu_2S bulk can act as the light absorber, which has been widely employed in photovoltaics, photocatalysis and solar energy conversion.[34,37–41] In particular, the great difference of the mobilities between electrons and holes of 2D Cu_2S[35] can dramatically reduce the possibility of the photo-induced carrier recombination and improve the photocatalytic efficiency of the CO_2RR.[42] Meanwhile, copper sulfide compounds could balance the binding strengths of the H* and CO* intermediates, respectively, i.e. the low-coordinated Cu surface atoms enhance CO* binding and S atoms suppress the HER, which hold promising prospects for boosting both the activity and product selectivity.[43,44]

In this work, we demonstrate that 2D β-Cu_2S and δ-Cu_2S monolayers are two promising photocatalysts for the CO_2RR into C_2H_5OH under visible light irradiation. Both catalysts possess strong adsorption ability for CHO* and CO* intermediates, resulting in a large deviation from the scaling relation of the transition-metal. Moreover, the strong CO* adsorption promotes an increase of local CO* coverage, which significantly reduces the limiting potential. The calculated potential-limiting steps for the whole CO_2RR process are no more than 0.50 eV, while those for the HER are as high as 1.53 and 0.87 eV. More importantly, the CHO–CO coupling only needs to overcome an ultra-low kinetic barrier of ∼0.3 eV, half of that on the Cu surface,[45,46] which facilitates the formation of CHOCO* and high selectivity for C_2H_5OH products. Besides, these catalysts also exhibit satisfactory visible light absorption and suitable band edge positions, which might be applied to CO_2 reduction under visible light irradiation.

Computational methods

All the density functional theory (DFT) calculations in this work were carried out using the Vienna Ab Initio Simulation Package (VASP).[47] The projector augmented wave potentials[48] was employed to describe the electron–ion interactions in the periodic system. The Perdew–Burke–Ernzerhof (PBE) functional within the generalized gradient approximation (GGA)[49] was utilized to treat the exchange–correlation interactions and the cutoff energy of 500 eV was selected for the plane-wave basis.[35,36] The convergence criteria for the electronic self-consistent iteration was set to 10^{-5} eV and the ionic relaxation continued until the maximum force on each atom was less than 0.02 eV Å^{-1}, which was updated by the conjugate gradient approach. In order to avoid the interaction between two periodic units, a 20 Å vacuum layer was added to all the slab models. The DFT-D3 method by Grimme et al.[50] was performed for the van der Waals correction. Ab initio molecular dynamics (AIMD) simulations were employed by using a $4 \times 4 \times 1$ supercell under the canonical ensemble lasting for 10 ps with a time step of 2.0 fs. The temperature was set to 800 K by using the Nóse–Hoover method.[51] Bader charge was calculated by using the Bader Charge Analysis script written by Henkelman and co-workers.[52] The electronic band structures and optical properties of β-Cu_2S and δ-Cu_2S monolayers were calculated accurately by using the Heyd–Scuseria–Ernzerhof hybrid (HSE06) functional.[53] All the C–C coupling barrier calculations were employed using the climbing image nudged elastic band (CI-NEB)[54] method. All the vibrational frequencies are positive except for one negative one, indicating that the transition state is a reliable first order saddle point. More details are given in the ESI.†

Results and discussion

Binding energies of the key reduction intermediates of CO* and CHO* scaling have been shown to be the bottleneck in CO_2RR activity for metallic catalysts.[21] By deviating from the above scaling relationship, CHO* can be stabilized over CO*, which can greatly reduce the potential determining step (PDS) for the CO* reduction into CHO*.[23,24] Fig. 1a depicts the high free energy change caused by the scaling relation between CHO* and CO*. The strong CO* adsorption promotes an increase of CO* coverage, which will significantly reduce the PDS by stabilizing CHO* and CO* on Cu_2S monolayers (Fig. 1b). Fig. 1c presents the binding energies of CHO* versus CO* on Cu_2S monolayers, as well as transition-metal (100) scaling relations. The detailed adsorption structure and binding energies of CHO* and CO* on Cu(100), β-Cu_2S and δ-Cu_2S are shown in Fig. S1 (ESI†). Clearly, both β-Cu_2S and δ-Cu_2S deviate from the scaling relation of the transition-metal (100),[21] which is expected to achieve dramatic reduction in PDS.

During the CO_2RR into CO*, two proton/electron pairs will be consumed through proton-coupled electron transfer with COOH* intermediate. However, the formation of HCOOH* and CO* products is competitive, because the COOH* intermediate can also be directly protonated into HCOOH*. Thus, it is very necessary to compare the product selectivity of HCOOH* and CO* when two proton/electron pairs are transferred. The adsorbed structures of COOH* and HCOO* intermediates are shown in Fig. 2a, including carbon coordination and oxygen
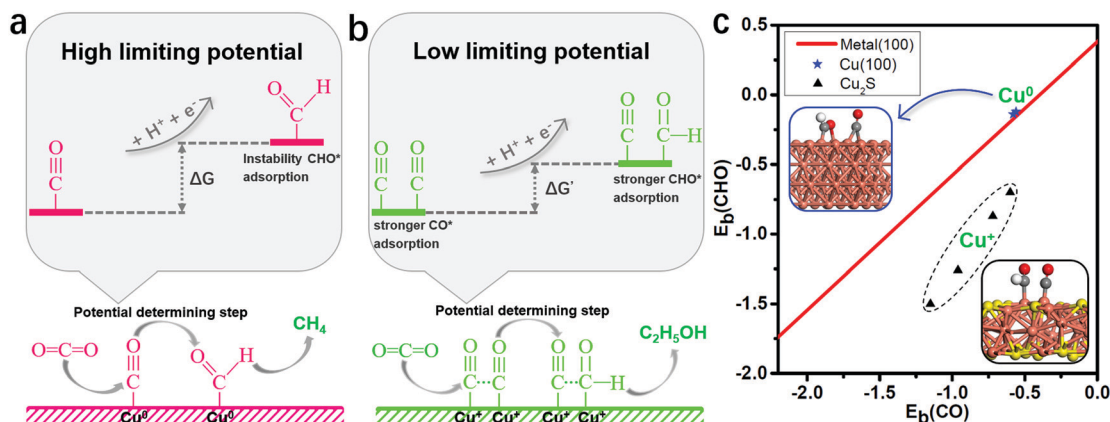
Fig. 1 (a) Schematic diagram of high free energy change caused by the scaling relationship between CHO* and CO*. (b) Reducing the free energy change by stabilizing CO* and CHO* on Cu_2S. (c) Binding energies of CHO* [E_b(CHO)] *versus* CO* [E_b(CO)] on Cu_2S, as well as the transition-metal (100) scaling relation. Cu, orange; S, yellow; C, grey; O, red and H, white. The detailed binding energy data of CHO* and CO* are given in the ESI.†

coordination. In Fig. 2b, the CO_2 protonation has two different pathways: (i) $CO_2 \rightarrow COOH^* \rightarrow CO^*$; (ii) $CO_2 \rightarrow HCOO^* \rightarrow HCOOH^*$. The optimized structures of the intermediates and corresponding hydrogenation free energies are plotted in Fig. S2 and Table S2 (ESI†), respectively. Clearly, the rate-determining step of $HCOO^* \rightarrow HCOOH^*$ needs to overcome a higher free energy barrier than that of $CO_2 \rightarrow COOH^*$ on δ-Cu_2S (0.46 *vs.* 0.21 eV, Fig. 2c) and β-Cu_2S (0.43 *vs.* 0.08 eV, Fig. 2d), then CO* can easily form due to the downhill free energy difference of $\Delta G_{COOH^* \rightarrow CO^*}$. In addition, the free energy of ΔG_{CO^*} is significantly lower than that of ΔG_{HCOOH^*} because

of the much stronger binding of CO on δ-Cu_2S and β-Cu_2S (the black line displayed in Fig. 2c and d). Therefore, the β-Cu_2S and δ-Cu_2S monolayers are desirable Cu-based catalysts for the CO_2RR with better selectivity to CO* rather than HCOOH*.

As the adsorption of intermediates is affected by the surface coverage of CO*, we explore the binding energies of these two catalysts under different CO* coverage. Fig. S3 (ESI†) shows the varying relationship between the CO* coverage ranging from 1/9 to 6/9 and the binding energies, and the catalysts binding 2CO* are the most stable (detailed adsorption configurations are shown in Fig. S4, ESI†). Under 2CO* coverage, the PDS for
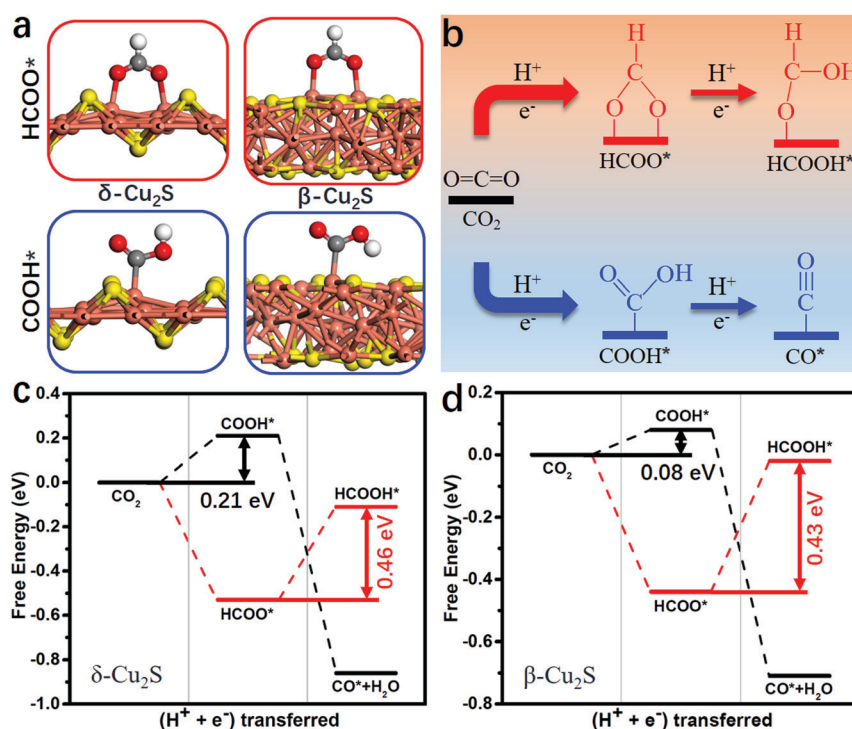

Fig. 2 (a) Optimized geometry of the intermediates of HCOO* and COOH* on δ-Cu_2S and β-Cu_2S. Cu, orange; S, yellow; C, grey; O, red and H, white. (b) The CO_2 protonation has two different pathways: (i) $CO_2 \rightarrow COOH^* \rightarrow CO^*$ (bottom path); (ii) $CO_2 \rightarrow HCOO^* \rightarrow HCOOH^*$ (top path). The free energy profiles of CO_2 hydrogenation into CO* and HCOOH* on (c) δ-Cu_2S and (d) β-Cu_2S when two proton/electron pairs ($2H^+/2e^-$) are transferred.
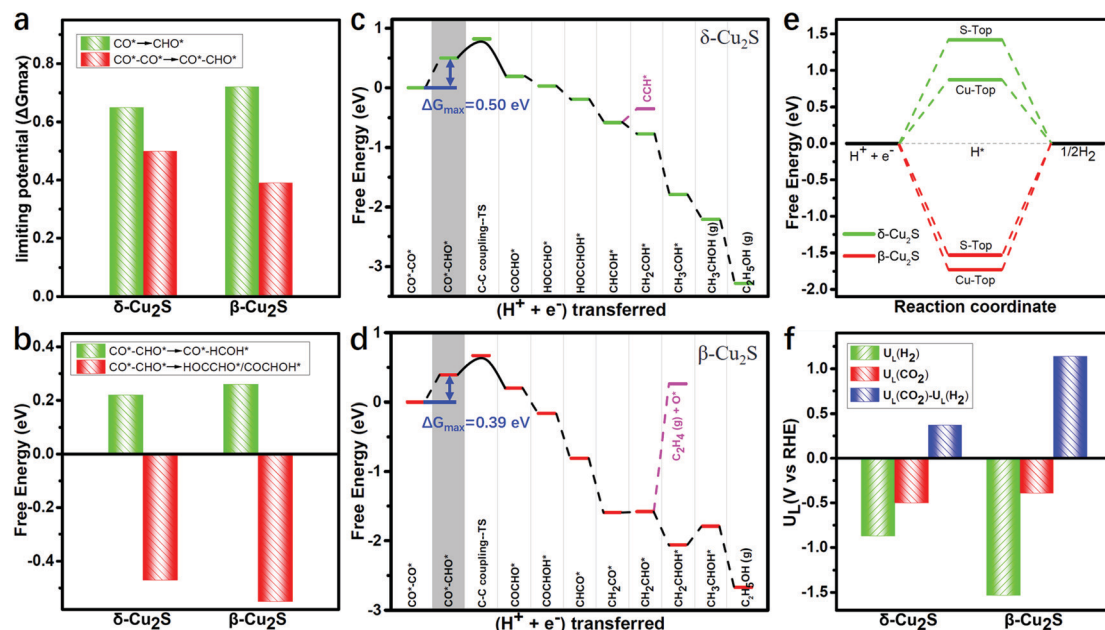
Fig. 3 Free energy of the hydrogenation step of (a) CO*–CO* → CO*–CHO* and CO* → CHO*, (b) CO*–CHO* → CO*–HCOH* and CO*–CHO* → HOCCHO*/COCHOH*. Free energy diagrams of CO*–CO* hydrogenation to C_2H_5OH on (c) δ-Cu_2S and (d) β-Cu_2S. Limiting potential is obtained from the maximum free energy change (ΔG_{max}) of the whole reaction process, which is marked by blue lines. (e) Free energy profiles of the HER on δ-Cu_2S (green line) and β-Cu_2S (red line). (f) Limiting potentials for the CO_2RR $U_L(CO_2)$, HER $U_L(H_2)$ and difference $U_L(CO_2) - U_L(H_2)$ on δ-Cu_2S and β-Cu_2S monolayers.

the CO* reduction into CHO* is significantly reduced to 0.39 and 0.50 eV (see Fig. 3a) on β-Cu_2S and δ-Cu_2S, respectively. This indicates that the stronger adsorption strength of CO* promotes the CO* coverage, and thereby reduces the PDS remarkably, which agrees well with the previous report on Cu_4@g-C_3N_4.[55]

Generally, CO*–CHO* is a vital intermediate in determining the selectivity between the C_1 and C_2 products, i.e. CH_3OH and C_2H_5OH. For C_1 products, the hydrogenation of CHO* → HCOH* only needs to overcome very low free energy barriers of 0.22 and 0.26 eV, which are much lower than that of CO* → CHO* (0.99 and 0.84 eV) on δ-Cu_2S and β-Cu_2S (Fig. S5, ESI†), respectively. In other words, the reduction of CHO* is relatively facile because the CHO* (sp^2 hybridization) has more p-character than the sp hybridized CO* (Fig. S6, ESI†). For C_2 products, the free energies of the hydrogenation of CO*–CHO* into HOCCHO*/COCHOH* on δ-Cu_2S and β-Cu_2S are −0.47 and −0.55 eV (Fig. 3b), respectively. Therefore, the formation of C_2 products becomes more favorable than that of the C_1 product since the former occurs spontaneously, while the latter is endothermic. In general, the energy of C sp^3 hybrid orbitals increases with the increase of p-character (see Fig. S6, ESI†), which makes the hydrogenation of CO*–CHO* → HOCCHO*/COCHOH* much easier than that of CO*–CHO* → CO*–HCOH* (Fig. S7, ESI†).

The full free energy profiles of the CO*–CO* hydrogenation to C_2H_5OH on δ-Cu_2S and β-Cu_2S are displayed in Fig. 3c and d, respectively, and the detailed adsorption structures of the intermediates are plotted in Fig. S8 (ESI†). The C–C coupling is crucial for C_2 products, which normally largely affects the faradaic efficiency for a C_2H_5OH product. Generally, C–C coupling has two major pathways: (i) CO–CO coupling; (ii) CO–CHO coupling.

For the CO–CO coupling pathway, OCCO* is automatically split into two separated CO* after full structure optimization, suggesting that the OCCO* is energetically unfavorable. For CO–CHO coupling, the calculated kinetic barriers are only 0.28 and 0.32 eV on β-Cu_2S and δ-Cu_2S (Fig. 4a), respectively, half of that on the Cu(100) surface[45,46] (0.74 eV). From the atomic structures of the initial, transition and final states of CHO–CO coupling, we can clearly see that the CHO*, CO* and OCCHO* are stabilized on Cu top sites due to the upshift of the Cu d-band center on the Cu_2S surface relative to the Cu(100) surface (Fig. 4b). In addition, Bader charge analysis reveals substantial charge, i.e., 0.34e, transfer from each copper to sulfur, resulting in a positively charged copper oxidation state. As mentioned above, the surface Cu^+ can modify the surface structure of copper(ı)-based catalysts, which leads to the change of binding strength between the adsorbate and catalyst, promoting the CHO–CO coupling reaction. The adsorption strength of CO* on Cu_2S (−0.6 to −1.15 eV) is relatively lower than that of Ni, Pt, Pd and Rh (−1.65 to −1.88 eV).[21] The mild adsorption strength may probably avoid CO poisoning and thereby promote the subsequent reaction of CO. Subsequently, the C_2H_5OH is easily formed due to the downhill free energy of COCHO* → C_2H_5OH on δ-Cu_2S, while the step of the CH_2CHOH* → CH_3CHOH* only needs to overcome a particularly low free energy barrier of 0.26 eV on β-Cu_2S. During the CO_2RR process, once the CH_2CHO* is formed, the reaction route bifurcates into ethylene and ethanol. As plotted in Fig. 3c and d, the C_2 species are more favorable to be reduced to ethanol than ethylene as the calculated free energy barrier of the latter is significantly higher than that of the former, indicating that the ethanol is the main product of the CO_2RR. Moreover, we find that
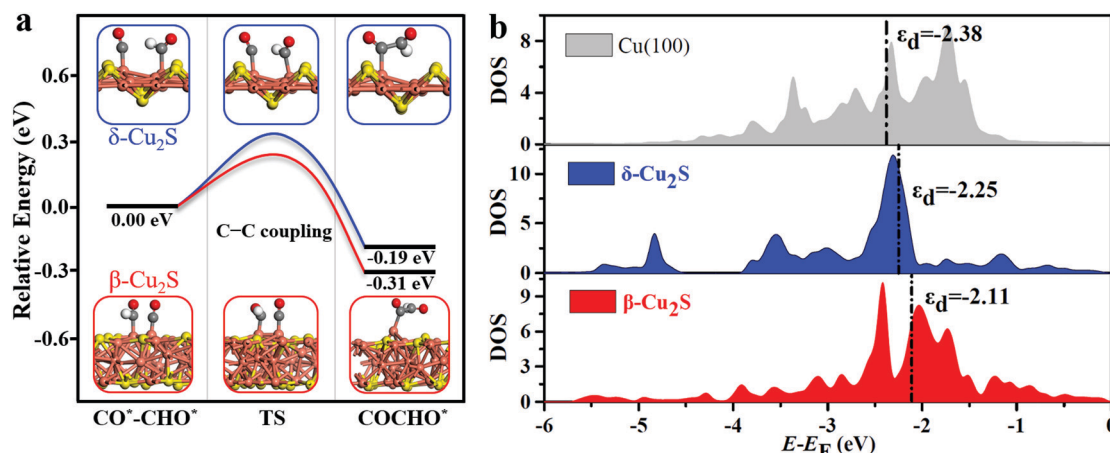
Fig. 4 (a) Relative energy diagram of the CHO−CO coupling processes on δ-Cu_2S and β-Cu_2S. Cu, orange; S, yellow; C, grey; O, red and H, white. (b) Density of states (DOS) of the *d*-band center (ε_d) on δ-Cu_2S, β-Cu_2S and Cu(100).

the free energy barrier decreases more for the formation of CH_2COH^*/CH_2CHOH^* (ethanol route) than that of CCH^*/C_2H_4 (ethylene route) with increasing CO^* coverage ranging from 2/9 to 6/9 ML (Fig. S9, ESI†). Therefore, the catalysts have relatively high selectivity for ethanol over ethylene.

Note that the above conclusions have been drawn based on the computational hydrogen electrode model, in which the effects of solvents are not explicitly considered. The effects of solvents may play an essential role in the largely affected chemical reactivity and the product selectivity of CO_2 reduction.[56] Besides, it can greatly reduce the C–C coupling kinetic barriers and improve the faradaic efficiency for C_2 products.[57] In the near future, we will further consider the influence of the effects of solvents to design efficient CO_2 reduction catalysts.

The above conclusion only considers the ground state DFT calculations. In order to further explore how the photoexcitation process drives the different reaction routes and thus the selectivity, the excited state DFT calculations were taken into account. We used the delta self-consistent field (ΔSCF) method for constrained DFT calculations[58] by promoting five spin-down electrons from the highest occupied to the spin-up lowest unoccupied molecular orbital at each *K* point.[59,60] As shown in Fig. S10 (ESI†), the Cu_2S catalysts have relatively high selectivity for ethanol over ethylene under excited state conditions, consistent with the ground state results. Therefore, the photoexcitation process has not changed the reaction routes and selectivity of the CO_2 reduction on Cu_2S.

Additionally, as the major competing reaction during the CO_2RR, the HER, which normally largely affects the faradaic efficiency for reduction reactions like CO_2RR and NRR, should also be considered. The H^* structures of two different adsorption sites and the corresponding free energy diagram of the HER are shown in Fig. S11 (ESI†) and Fig. 3e, respectively. Clearly, the Gibbs free energy barriers of the HER (1.53 eV and 0.87 eV) are significantly higher than those of the potential determining step barriers of CO_2RR (0.39 eV and 0.50 eV) on β-Cu_2S and δ-Cu_2S, indicating the high suppressing effect on the HER during the CO_2RR. The difference $[\Delta U_L(CO_2) - U_L(H_2)]$ between the limiting potentials for CO_2RR $U_L(CO_2)$ and HER $U_L(H_2)$ can reasonably

describe the CO_2RR selectivity, where a more positive $U_L(CO_2) - U_L(H_2)$ value means a higher selectivity toward the CO_2RR over the HER.[61,62] As shown in Fig. 3f, the β-Cu_2S and δ-Cu_2S have positive $U_L(CO_2) - U_L(H_2)$ values, indicative of the higher selectivity for the CO_2RR against the HER.

As a good photocatalyst, the catalyst should also have a satisfactory band gap value to efficiently absorb visible light. As shown in Fig. 5a and b, the direct band gap of β-Cu_2S at the Γ point is 1.45 eV, which is slightly larger than the value of 1.24 eV for δ-Cu_2S. The satisfactory band gap values indicate that these two catalysts can effectively absorb visible (VI) light and ultraviolet (UV) light. As plotted in Fig. 5c, the absorption spectra of β-Cu_2S and δ-Cu_2S show remarkably high absorption coefficients (10^5 cm^{-1}) under the irradiation of the full spectrum. For β-Cu_2S, there is a high intensity of absorption VI and UV light. In particular, the first and second absorption peaks are located at 1.95 eV and 3.89 eV, respectively, in good accordance with the experimental results.[38,63] In addition, the δ-Cu_2S monolayer with a wide optical absorption range can be utilized and the intense absorption band is centered at 1.50 eV in the infrared (IR) region. Moreover, previous studies showed that β-Cu_2S and δ-Cu_2S both have fairly large electron mobilities,[35] suggesting that the photo-generated electron and hole pairs will quickly reach the surface of these two catalysts to participate in the CO_2RR. Meanwhile, the great difference between the electron and hole effective mass on the catalysts will dramatically reduce the possibility of photo-induced carrier recombination as well, which should further facilitate the photocatalytic efficiency of the CO_2RR.

As a photocatalyst for CO_2 reduction, the semiconductor should have satisfactory band edge positions to match the potentials of CO_2 reduction and H_2O oxidation as well. According to the above obtained band gaps (Fig. 5a and b), the electronic band structures *versus* normal hydrogen electrode (NHE) potential at pH = 7 can be elucidated. As manifested in Fig. 5d, the conduction band minima (CBMs) of β-Cu_2S and δ-Cu_2S are more negative than the redox potentials of CO_2/C_2H_5OH (−0.33 V *vs.* NHE),[42] suggesting that photo-generated
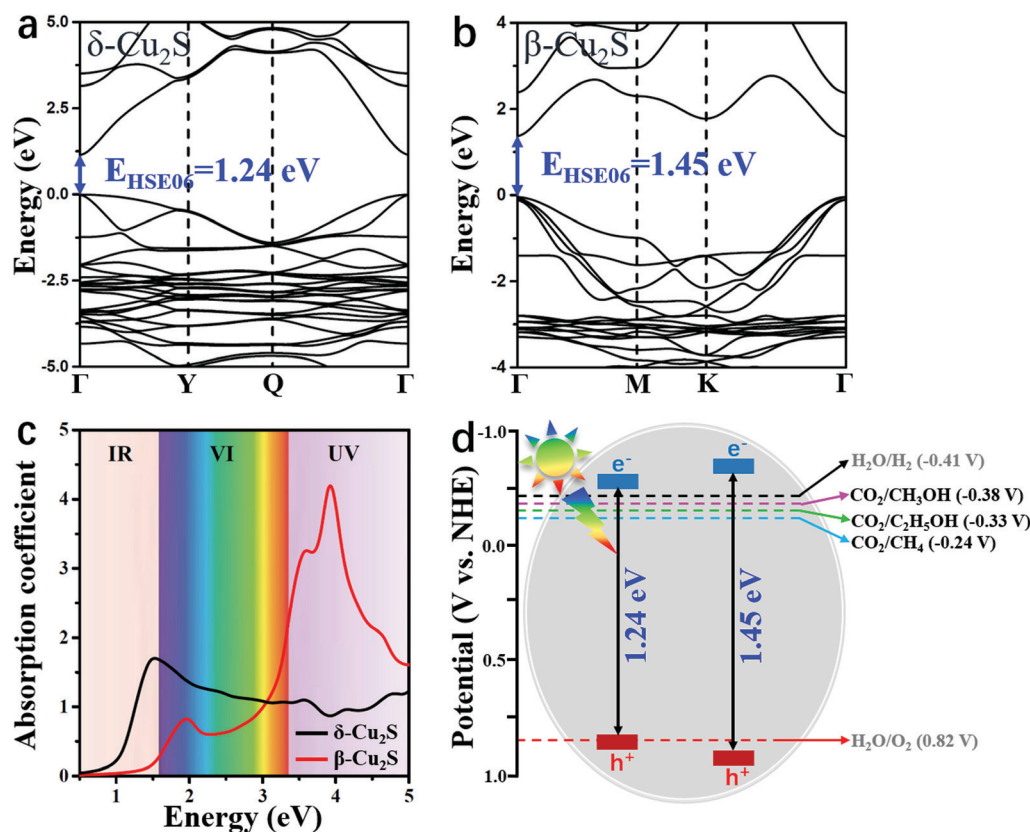
Fig. 5 Electronic band structure of (a) δ-Cu_2S and (b) β-Cu_2S with a direct band gap at the Γ point. (c) Optical absorption spectra of β-Cu_2S and δ-Cu_2S are indicated by red and black lines, respectively. (d) Schematic illustration of the band edge positions of β-Cu_2S and δ-Cu_2S relative to NHE at pH = 7. The calculations were performed by HSE06.

electrons have sufficiently high reducing power and can be utilized as photocatalysts for the CO_2RR to C_2H_5OH. Meanwhile, the valence band maximum (VBM) is below the H_2O/O_2 potential[3] (0.82 V *vs.* NHE) and the high oxidation ability of the hole carriers enables H_2O splitting and generates H^+ for the CO_2RR. These results indicate that β- and δ-Cu_2S monolayers possess suitable band gaps as well as appropriate band edge positions, and can act as promising photocatalysts for the CO_2RR into C_2H_5OH. In fact, previous studies have shown that the Cu_2S bulk is excellent for oxygen evolution reaction activity and durability, and has been widely used in water splitting to produce H^+.[64–66] Therefore, we deduce that β-Cu_2S and δ-Cu_2S monolayers that have the merits of satisfactory band edge position and visible light absorption properties, and highly active surface are promising photocatalysts for the CO_2RR.

In addition, we have further evaluated the stability of the catalysts. The δ-Cu_2S and β-Cu_2S have tetragonal and hexagonal structures, respectively, as shown in Fig. S12a and b (ESI†). In AIMD simulations, in which the time step was set to be 2.0 fs for a total period of 10 ps, the energy and temperature fluctuations with time evolution oscillate near the equilibrium state and the atomic configurations remain very well at the experimental synthesis temperature of β-Cu_2S ($\sim$800 K)[33] (Fig. S12c and d, ESI†). In fact, as pointed out above, the ultrathin 2D β-phase Cu_2S bilayer has been successfully synthesized in the laboratory[32–34]

and a 2D δ-phase Cu_2S monolayer has also been predicted theoretically with superior oxidation resistance in the air and moisture atmosphere.[35] More importantly, during the process of photochemical CO_2RR, the structure still maintains stability under the existence of the solvent and potential (see Fig. S13, ESI†). These results suggest the high structural stability and a large experimental feasibility for Cu_2S based catalysts.

Conclusions

In summary, we have demonstrated that 2D β-Cu_2S and δ-Cu_2S monolayers, as promising highly efficient photocatalytic semiconductor materials, can efficiently achieve the hydrogenation of CO_2 to C_2H_5OH under the irradiation of visible-light. Our DFT calculations suggest that the β-Cu_2S and δ-Cu_2S photocatalysts can not only greatly suppress the competing HER, but also break the scaling relations in the multi-intermediates to increase CO* coverage and reduce the potential-limiting steps of CO* → CHO*. More importantly, the CHO–CO coupling only needs to overcome a very low kinetic barrier of 0.28 and 0.32 eV, and COCHO* is recognized as the key intermediate for C_2 formation, resulting in a high selectivity for C_2H_5OH on both β-Cu_2S and δ-Cu_2S. Moreover, these two catalysts also exhibit satisfactory band edge positions and visible light absorption for

the photocatalytic CO_2RR and high thermodynamic stability over 800 K. Low limiting potential, high product selectivity, good thermal stability and strong visible light absorbance make Cu_2S a very attractive photocatalyst for the CO_2RR, which may provide new insights into the development of novel semiconductor photocatalysts.

Conflicts of interest

The authors declare no competing financial interest.

Acknowledgements

References

1 J. Ran, M. Jaroniec and S. Z. Qiao, *Adv. Mater.*, 2018, **30**, 1704649.
2 Y. Zhao, G. I. N. Waterhouse, G. Chen, X. Xiong, L. Z. Wu, C. H. Tung and T. Zhang, *Chem. Soc. Rev.*, 2019, **48**, 1972–2010.
3 X. Li, J. Yu, M. Jaroniec and X. Chen, *Chem. Rev.*, 2019, **119**, 3962–4179.
4 J. Di, *et al.*, *Nat. Commun.*, 2019, **10**, 2840.
5 X. Li, L. Liang, Y. Sun, J. Xu, X. Jiao, X. Xu, H. Ju, Y. Pan, J. Zhu and Y. Xie, *J. Am. Chem. Soc.*, 2019, **141**, 423–430.
6 U. Ulmer, T. Dingle, P. N. Duchesne, R. H. Morris, A. Tavasoli, T. Wood and G. A. Ozin, *Nat. Commun.*, 2019, **10**, 3169.
7 X. Li, Y. Sun, J. Xu, Y. Shao, J. Wu, X. Xu, Y. Pan, H. Ju, J. Zhu and Y. Xie, *Nat. Energy*, 2019, **4**, 690–699.
8 J. Chen, J. Yin, X. Zheng, H. Ait Ahsaine, Y. Zhou, C. Dong, O. F. Mohammed, K. Takanabe and O. M. Bakr, *ACS Energy Lett.*, 2019, **4**, 1279–1286.
9 B. Zhou, *et al.*, *Energy Environ. Sci.*, 2019, **12**, 2842–2848.
10 T. Yan, L. Wang, Y. Liang, M. Makaremi, T. E. Wood, Y. Dai, B. Huang, A. A. Jelle, Y. Dong and G. A. Ozin, *Nat. Commun.*, 2019, **10**, 2521.
11 X. Wu, Y. Li, G. Zhang, H. Chen, J. Li, K. Wang, Y. Pan, Y. Zhao, Y. Sun and Y. Xie, *J. Am. Chem. Soc.*, 2019, **141**, 5267–5274.
12 C. G. Morales-Guio, *et al.*, *Nat. Catal*, 2018, **1**, 764–771.
13 T.-T. Zhuang, *et al.*, *Nat. Catal*, 2018, **1**, 421–428.
14 E. Bertheussen, *et al.*, *Angew. Chem., Int. Ed.*, 2016, **128**, 1472–1476.
15 S. Sorcar, Y. Hwang, C. A. Grimes and S.-I. In, *Mater. Today*, 2017, **20**, 507–515.
16 B. AlOtaibi, S. Fan, D. Wang, J. Ye and Z. Mi, *ACS Catal.*, 2015, **5**, 5342–5348.
17 Z. Jiang, *et al.*, *Energy Environ. Sci.*, 2018, **11**, 2382–2389.
18 D. Voiry, H. S. Shin, K. P. Loh and M. Chhowalla, *Nat. Rev. Chem.*, 2018, **2**, 0105.
19 K.-H. Liu, H.-X. Zhong, S.-J. Li, Y.-X. Duan, M.-M. Shi, X.-B. Zhang, J.-M. Yan and Q. Jiang, *Prog. Mater. Sci.*, 2018, **92**, 64–111.
20 I. Shown, *et al.*, *Nano Lett.*, 2014, **14**, 6097–6103.
21 Y. Li and Q. Sun, *Adv. Energy Mater.*, 2016, **6**, 1600463.
22 H.-K. Lim, H. Shin, W. A. Goddard, Y. J. Hwang, B. K. Min and H. Kim, *J. Am. Chem. Soc.*, 2014, **136**, 11355–11361.
23 X. Hong, K. Chan, C. Tsai and J. K. Nørskov, *ACS Catal.*, 2016, **6**, 4428–4437.
24 S. B. Varandili, J. Huang, E. Oveisi, G. L. De Gregorio, M. Mensi, M. Strach, J. Vavra, C. Gadiyar, A. Bhowmik and R. Buonsanti, *ACS Catal.*, 2019, **9**, 5035–5046.
25 J. Zeng, W. Zhang, Y. Yang, D. Li, X. Yu and Q. Gao, *ACS Appl. Mater. Interfaces*, 2019, **11**, 33074–33081.
26 A. Bhowmik, H. A. Hansen and T. Vegge, *ACS Catal.*, 2017, **7**, 8502–8513.
27 H. Mistry, *et al.*, *Nat. Commun.*, 2016, **7**, 12123.
28 K. P. Kuhl, E. R. Cave, D. N. Abram and T. F. Jaramillo, *Energy Environ. Sci.*, 2012, **5**, 7050–7059.
29 Z. Q. Liang, *et al.*, *Nat. Commun.*, 2018, **9**, 3828.
30 Q. Zhu, X. Sun, D. Yang, J. Ma, X. Kang, L. Zheng, J. Zhang, Z. Wu and B. Han, *Nat. Commun.*, 2019, **10**, 3851.
31 H. Jung, S. Y. Lee, C. W. Lee, M. K. Cho, D. H. Won, C. Kim, H.-S. Oh, B. K. Min and Y. J. Hwang, *J. Am. Chem. Soc.*, 2019, **141**, 4624–4633.
32 B. Li, L. Huang, G. Zhao, Z. Wei, H. Dong, W. Hu, L. W. Wang and J. Li, *Adv. Mater.*, 2016, **28**, 8271–8276.
33 F. B. Romdhane, O. Cretu, L. Debbichi, O. Eriksson, S. Lebegue and F. Banhart, *Small*, 2015, **11**, 1253–1257.
34 R. Shahzad, T. Kim, J. Mun and S. W. Kang, *Nanotechnology*, 2017, **28**, 505601.
35 Y. Guo, Q. Wu, Y. Li, N. Lu, K. Mao, Y. Bai, J. Zhao, J. Wang and X. C. Zeng, *Nanoscale Horiz.*, 2019, **4**, 223–230.
36 J. Yu, T. Li, G. Nie, B. P. Zhang and Q. Sun, *Nanoscale*, 2019, **11**, 10306–10313.
37 A. B. Wong, S. Brittman, Y. Yu, N. P. Dasgupta and P. Yang, *Nano Lett.*, 2015, **15**, 4096–4101.
38 Q. Cao, R. Che and N. Chen, *Appl. Catal., B*, 2015, **162**, 187–195.
39 J.-Y. Li, L. Yuan, S.-H. Li, Z.-R. Tang and Y.-J. Xu, *J. Mater. Chem. A*, 2019, **7**, 8676–8689.
40 A. Manzi, T. Simon, C. Sonnleitner, M. Doblinger, R. Wyrwich, O. Stern, J. K. Stolarczyk and J. Feldmann, *J. Am. Chem. Soc.*, 2015, **137**, 14007–14010.
41 P. Kar, S. Farsinezhad, X. Zhang and K. Shankar, *Nanoscale*, 2014, **6**, 14305–14318.
42 X. Chang, T. Wang and J. Gong, *Energy Environ. Sci.*, 2016, **9**, 2177–2196.
43 T. Shinagawa, G. O. Larrazábal, A. J. Martín, F. Krumeich and J. Pérez-Ramírez, *ACS Catal.*, 2018, **8**, 837–844.
44 Y. Deng, Y. Huang, D. Ren, A. D. Handoko, Z. W. Seh, P. Hirunsit and B. S. Yeo, *ACS Appl. Mater. Interfaces*, 2018, **10**, 28572–28581.
45 J. D. Goodpaster, A. T. Bell and M. Head-Gordon, *J. Phys. Chem. Lett.*, 2016, **7**, 1471–1477.
46 H. Zhang, Y. Zhang, Y. Li, S. Ahn, G. T. R. Palmore, J. Fu, A. A. Peterson and S. Sun, *Nanoscale*, 2019, **11**, 12075–12079.

47 G. Kresse and J. Furthmüller, *Phys. Rev. B: Condens. Matter Mater. Phys.*, 1996, **54**, 11169–11186.

48 P. E. Blöchl, *Phys. Rev. B: Condens. Matter Mater. Phys.*, 1994, **50**, 17953–17979.

49 J. P. Perdew, J. A. Chevary, S. H. Vosko, K. A. Jackson, M. R. Pederson, D. J. Singh and C. Fiolhais, *Phys. Rev. B: Condens. Matter Mater. Phys.*, 1992, **46**, 6671–6687.

50 L. A. Burns, A. Vazquez-Mayagoitia, B. G. Sumpter and C. D. Sherrill, *J. Chem. Phys.*, 2011, **134**, 084107.

51 S. Nosé, *J. Chem. Phys.*, 1984, **81**, 511–519.

52 G. Henkelman, A. Arnaldsson and H. Jónsson, *Comput. Mater. Sci.*, 2006, **36**, 354–360.

53 J. Heyd, G. E. Scuseria and M. Ernzerhof, *J. Chem. Phys.*, 2003, **118**, 8207–8215.

54 G. Henkelman, B. P. Uberuaga and H. Jónsson, *J. Chem. Phys.*, 2000, **113**, 9901–9904.

55 X. Bai, Q. Li, L. Shi, X. Niu, C. Ling and J. Wang, *Small*, 2020, **16**, 1901981.

56 X. Zhao and Y. Liu, *J. Am. Chem. Soc.*, 2020, **142**, 5773–5777.

57 J. H. Montoya, C. Shi, K. Chan and J. K. Nørskov, *J. Phys. Chem. Lett.*, 2015, **6**, 2032–2037.

58 J. Gavnholt, T. Olsen, M. Engelund and J. Schiøtz, *Phys. Rev. B: Condens. Matter Mater. Phys.*, 2008, **78**, 075441.

59 Y. Zhao, *et al.*, *Adv. Mater.*, 2018, **30**, 1803127.

60 W. Gao, *et al.*, *Chem.*, 2018, **4**, 2917–2928.

61 D. Kim, C. Xie, N. Becknell, Y. Yu, M. Karamad, K. Chan, E. J. Crumlin, J. K. Norskov and P. Yang, *J. Am. Chem. Soc.*, 2017, **139**, 8329–8336.

62 W. Bi, X. Li, R. You, M. Chen, R. Yuan, W. Huang, X. Wu, W. Chu, C. Wu and Y. Xie, *Adv. Mater.*, 2018, **30**, 1706617.

63 Y. Wu, C. Wadia, W. Ma, B. Sadtler and A. P. Alivisatos, *Nano Lett.*, 2008, **8**, 2551–2555.

64 Y. He, *et al.*, *Nat. Mater.*, 2019, **18**, 1098–1104.

65 L. He, D. Zhou, Y. Lin, R. Ge, X. Hou, X. Sun and C. Zheng, *ACS Catal.*, 2018, **8**, 3859–3864.

66 L. An, P. Zhou, J. Yin, H. Liu, F. Chen, H. Liu, Y. Du and P. Xi, *Inorg. Chem.*, 2015, **54**, 3281–3289.